THE ASTROPHYSICAL JOURNAL, 411:708–719, 1993 July 10

MAGNETIC FIELDS IN MASSIVE CLOUD CORES: COMPARISON OF MILLIPOL AND *IRAS* RESULTS

BRIAN D. KANE AND DAN P. CLEMENS
Astronomy Department, Boston University, 725 Commonwealth Avenue, Boston, MA 02215

RICHARD BARVAINIS
Haystack Observatory, NEROC, Route 40, Westford, MA 01886

AND

ROBERT W. LEACH
Astronomy Department, College of Sciences, San Diego State University, San Diego, CA 92182-0334
Received 1992 October 22; accepted 1993 January 15

ABSTRACT

We present new results of 1300 μm polarimetry obtained with 30″ resolution toward 10 cloud cores, of which seven were detected, using the MILLIPOL polarimeter. The detected cores are associated with compact H II regions in the massive molecular clouds DR 21, OMC-1, Sagittarius B2, W3, W49, and W51. Upper limits were obtained for the cores in W3, NGC 6334, and M17. The polarization directions inferred from MILLIPOL measurements are compared to resolution-enhanced *IRAS* co-added data in order to investigate the interaction of the embedded magnetic field with the dust in these massive cloud cores. Specifically, maps of dust temperatures inferred from 60/100 μm flux ratios and maps of 100 μm dust opacities are compared to the MILLIPOL-traced polarization directions of these cores.

Determinations of cloud core axis ratios and position angles were performed by examining the morphologies of *IRAS*-traced dust opacity structures. The MILLIPOL-detected cloud cores show core axis ratios ranging from $\sim$1.5 to 3.2. The difference angles between the major axis position angles of the dust structures and the directions of the MILLIPOL polarization position angles for the detected cores have a mean value of $-2°$, with a dispersion of $\sim 17°$. Hence the magnetic field is found to be generally perpendicular to the core dust distributions. The cloud cores detected by MILLIPOL are cooler ($\langle T \rangle \sim 43$ K), and significantly more opaque at 100 μm ($\tau > 0.005$) than the nondetected cores ($\langle T \rangle \sim 50$ K, $\tau < 0.007$).

Subject headings: H II regions — ISM: clouds — ISM: magnetic fields — polarization

1. INTRODUCTION

What is the extent to which magnetic fields affect or control the star formation process? Do magnetic fields help to flatten rotating and nonrotating dense cloud cores? Do they help to collimate bipolar outflows from young stellar objects with dusty accretion disks? What might be the effect of massive star formation on the uniformity of the magnetic field over typical scales of several tenths of a parsec? The answers to these questions can be sought by studying the polarized emission and the spatial distribution of dust contained in regions of star formation.

Studying dust distributions is important for determining the nature of the stellar sources of radiation (Chini et al. 1986a, b, c), and the physical nature of dense cloud cores (Schloerb, Snell, & Schwartz 1987, hereafter SSS; Gordon & Jewell 1987, hereafter GJ). In examining the 1300 μm emission from dust associated with bright H II regions, GJ have found that millimeter brightness distributions are often different from their far-infrared counterparts. Thus, a complementary far-infrared study of dust distributions is necessary to more fully comprehend the nature of the dust temperature and opacity. Characterizing the polarization of dust emission is an important way of constraining the properties of the magnetic field which may penetrate and surround these dusty cores. The onset of bipolar outflows from young stellar objects is poorly understood and may be related to the formation of an accretion disk in the presence of a magnetic field. A morphological correlation of outflow directions with magnetic field directions and with the orientations of elongated dusty dense cores could help assess the importance of the field. In addition, the connection between magnetic fields and cloud fragmentation and collapse can be addressed via similar morphological correlations.

Generally the magnetic field *strength* can only be measured via the Zeeman effect (for example, Troland et al. 1986, Heiles 1988), which is most easily detected in low-density H I or OH gas. In the dense cores where star formation proceeds, Zeeman experiments may not be possible because molecular spectral line frequency splittings are much smaller than the typical line widths encountered. While the magnetic field strength in these cloud cores cannot currently be measured during the crucial period of dense core formation and protostellar collapse, the magnetic field *direction* is routinely measured via the polarization of starlight by elongated dust grains spinning about magnetic field lines (Davis & Greenstein 1951). These grains are expected to also emit linearly polarized radiation generated as a result of thermal radiation emitted as an excess parallel to the major axis of the grains (Hildebrand 1988). The direction of this polarization is perpendicular to the local magnetic field (as opposed to the case of optical polarization induced by anisotropic *absorption*, where magnetic field directions and polarization directions are parallel).

The proximity and brightness of the Orion cloud core made it a natural first choice for study. Barvainis, Clemens, & Leach (1988, hereafter BCL) used MILLIPOL to make the first detection of linear polarization at 1300 μm toward Orion, finding that the BN/KL region was polarized at the few percent level.

Using a different polarimeter and telescope combination, Novak, Predmore, & Goldsmith (1990) confirmed the BCL observations at 1300 μm. Subsequently, we (Leach et al. 1991, hereafter L91) used MILLIPOL to map the 1300 μm emission at 15 positions across the core of OMC-1 and found a very uniform magnetic field direction: the angular dispersion of the polarization directions was 9°. The mean Orion percentage polarization was quite high ($\sim$4.6%) and tended to increase away from the cloud core. The dip in percentage polarization toward BN/KL can best be explained by the combined effect of a change of the line-of-sight component of the magnetic field, in conjunction with field line tangling.

Submillimeter and far-infrared observations of Orion have also been performed by Hildebrand and collaborators using the KAO (Hildebrand, Dragovan, & Novak 1984; Dragovan 1986; Novak et al. 1989, hereafter N89; Gonatas et al. 1990, hereafter G90). All of these studied the Kleinmann-Low (KL) nebula, and the far-infrared emission peak $\sim$1'.5 south of KL. Their far-infrared polarimetric measurements generally agree with the MILLIPOL and optical measurements, indicating a common implied field direction. In OMC-1, the uniformity in field direction across a large scale ($\sim$0.3 pc) suggests the possible importance of the field in helping to order the cloud core structure. The Orion molecular ridge is roughly perpendicular to the field direction, while both the rotation axis and the high-velocity outflow from BN/KL are parallel to the field direction.

G90 found similar results in their mapping study of Orion at 100 μm. They found that the position angles of polarization were well ordered, suggesting the presence of a large-scale magnetic field of strength between 0.7 and 4 mG which is embedded in a dense region of the cloud. Their mean polarization percentage was also quite high ($\sim$3.7%), and showed a somewhat weaker dip toward the BN/KL region. They suggested that the large variation in the magnitude of polarization may reflect the composition and/or shape of the dust grains at different positions toward the cloud core.

N89 also published detection of polarized far-infrared (100 μm) radiation from dust in the clouds Mon R2 (one position) and Sagittarius A (five positions), and set upper limits for six other clouds, including W49 and W51. In Mon R2, they found that the field direction implied by their measurements did not agree with that implied by near-infrared polarimetry of embedded sources.

The number of cloud cores with measured millimeter, submillimeter, and far-infrared linear polarizations is quite small. At millimeter wavelengths, OMC-1 has the largest mean polarized emission of $\sim$4% (BCL; L91; N89; G90; Novak, Predmore, & Goldsmith 1990); Tamura et al. (1993) have reported a 1100 μm polarization of almost 3% toward IRAS 16293$-$2422. At submillimeter wavelengths, percentage polarizations of Mon R2 and Sagittarius A are on the order of 1%–2% (N89; Aitken et al. 1986). Upper limits, all less than 1%, have been set for six other clouds, including W49 and W51 (N89; Cudlip et al. 1982). At far-infrared wavelengths, Platt et al. (1991, hereafter P91) reported 100 μm array polarimetry of W3 (five positions: four probable detections, one upper limit) and W51 (six positions: five probable detections, one upper limit), with average percentage polarizations of $\sim$1% for W3 and 1%–2% for W51.

Several factors limit the rate of progress in detecting dust polarization. Typically, low dust temperatures of 20–50 K produce blackbody emission peaking at wavelengths from 60 to 150 μm, which do not easily penetrate our atmosphere. Airborne far-infrared observations have therefore been the most fruitful method of extracting accurate polarization information. Observations can be made longward of far-infrared wavelengths, but at the expense of diminished flux, and only shortward of those longer wavelengths where contamination from free-free emission generated near embedded massive stars becomes important ($\sim\lambda = 3$ mm; Gordon et al. 1986). GJ found that typically $\lambda = 3.5$ mm free-free emission peaks were not spatially coincident with the $\lambda = 1.3$ mm dust emission peaks for our cloud core sample. Most cloud cores in our sample were separated by more than one beamwidth from the corresponding free-free emission peaks and had less than $\sim$10% contamination due to free-free emission; toward W51, where the separation is only about one-half of a beamwidth, GJ estimated that the contribution of the free-free flux was only $\sim$ 15% of the total flux in the beam. Because the systematic total flux uncertainties here and those of GJ are of the order of 15%–20%, the contamination of free-free flux and dilution of polarization percentage by this unpolarized component in the MILLIPOL beam is not statistically significant. Since radio telescopes are typically much larger than far-infrared or submillimeter telescopes, observations conducted at millimeter wavelengths can minimize the problems of diminished flux and coarse angular resolution. Also, although *IRAS* observations at 60 and 100 μm are suitable for the study of the temperature and opacity distributions of dust in massive cloud cores, they are inadequate for independently addressing the effects of embedded magnetic fields on these distributions. But, deconvolution of *IRAS* images has allowed the comparison of dust opacity structures on angular scales similar to the size of the MILLIPOL beam.

In this paper we present results of new millimeter polarimetry of 10 cloud cores using the MILLIPOL polarimeter. Seven out of 10 cloud cores were detected (four 3 σ and three 2 σ detections), with polarized fluxes greater than $\sim$0.2 Jy per beam; the other three sources had polarized flux upper limits of $\sim$1–2 Jy per beam. We also present dust opacity maps constructed from 60 and 100 μm *IRAS* images which have been spatially enhanced by about a factor of 2. We find that 86% (six of seven) of our detected cores have dust structures whose major axes lie roughly parallel to their millimeter polarization vectors (perpendicular to the embedded magnetic fields); one has an elongation roughly perpendicular to its polarization vector.

In § 2 the observational methods of obtaining polarimetry using MILLIPOL are described, and the results are tabulated. In § 3 our resolution enhancement of the *IRAS* co-added survey images is described. In § 4 findings concerning each source, and correlations in our sample, are discussed. In § 5 the correlations found between embedded dust structures and magnetic fields are summarized, and the possible effects of the magnetic field in collimating outflows and in ordering cloud core structures are discussed.

2. MILLIPOL OBSERVATIONS

Polarimetry of the 1300 μm thermal dust emission toward embedded dense cloud cores was obtained using the MILLIPOL polarimeter (BCL; Clemens et al 1990, hereafter C90) on the NRAO 12 m telescope on Kitt Peak, Arizona, during 1988 April 1–6, and 1989 January 19–24. MILLIPOL consisted of a spinning, grooved, rexolite half-wave plate, analog and digital signal-processing electronics, and a data-collection computer.

MILLIPOL operated in front of the wire grid beam splitter, twin cooled-Schottky receivers, and dual-channel receiver normally used for continuum observations. The detected signal bandwidth was 600 MHz. Representative double-sideband system temperatures were 670 K (channel A) and 970 K (channel B) for the 1988 observations, and 600 K (channel A) and 580 K (channel B) for 1989.

During polarimetric observations, the half-wave plate was rotated at 6.25 Hz, for an effective polarization switching rate of 25 Hz. Data from the continuum receivers were integrated and collected every 800 μs. Each polarimetric scan consisted of five repetitions of 30 s duration spent on-source followed by 30 s duration toward a reference position, which was chosen to lie 34 s of right ascension eastward of the source position (up to 7'.5 away). Hence, reference observations traversed the same sections of sky and dome previously traversed by the source observations. Data were simultaneously collected in the two orthogonal polarizations. Total fluxes were obtained using beam chopping with 4'–6' beam throws and were calibrated via planetary observations. Separate day and night calibrations were maintained (C90) to account for thermal and solar illumination effects on the 12 m primary and the secondary support legs. Focusing was checked frequently, and pointing accuracy was maintained by frequent checks of Jupiter, Saturn, Venus, and Mars. The measured half-power beam width was 30", as determined by scans across the disks of Jupiter, Saturn, and Venus. Zenith opacities were measured via telescope dips every 2–3 hr and were in the range from 0.1 to 0.4. The instrumental polarization was determined to be at or below the 0.2% level, and the polarimetric sensitivity limit was demonstrated to be of the order of 0.03%, via observation of the polarized flux of the radiation belts of Jupiter (C90).

Polarimetric data were obtained in groups of $\sim$10 5 minute-duration scans to minimize source parallactic angle changes. In addition, observations were collected for identical, but opposite parallactic angles for each source to minimize systematic effects. Individual scans consisted of 40 data values of the on-source minus off-source flux versus polarimeter phase (0–2π). Each scan was plotted and examined for the presence of strong spikes, 60 Hz pickup, or strong gradients with polarimeter phase. These bad scans ($\leq$10%) were eliminated from further analysis. The raw data for a 10 scan group were averaged together using equal weighting. These averaged data for each of the two receiver channels were then fitted with a pair of sine waves to determine the Stokes U and Q parameters and their uncertainties. These parameters were corrected for the measured instrumental polarization (less than 0.2%; C90), the polarimeter zero phase offset angle determined from lunar limb calibrations (see BCL; C90), and the measured angular offset between the two receiver feed horns. These Stokes U and Q values (one pair for each 10 scan set) were then averaged across all the 10 scan sets for each source, weighted by the inverse square of the uncertainty for each set. From these global averages, the source polarizations P and position angles χ measured in each receiver channel (A and B) were obtained.

For observations made during 1988, the B channel data were judged to be not consistently reliable because of a difficulty in keeping both continuum receiver outputs within the capture range of the MILLIPOL electronics. We elected to keep the A channel data within range, partially at the expense of the B channel data. Through the separate averaging technique described above, however, most of the B channel Stokes parameters were found to be within 2 σ of their A channel counterparts. For those cases, the previously determined A and B channel Stokes parameter fits were then averaged together, weighted by the inverse squares of their uncertainties (which still favored the A channel data).

Table 1 presents the source list and final calibrated polarimetric data. Additional polarization data for Orion, also obtained during the same observing runs, are from L91. Column (1) lists the names for the observed cloud cores, with parenthetical notations reflecting terminology used in this paper. Columns (2) and (3) list coordinates for beam centers of each source observed, with the exception of Orion, for which coordinates denote the central position in the 15 position map from L91. Column (4) lists the total fluxes measured in the 30" beams. Column (5) lists the percentage polarization and uncertainty in polarization, with 2 σ upper limits for three sources. Uncertainties are internal in that they do not reflect total flux calibration uncertainties ($\sim$20%). Column (6) lists polarization position angles and their uncertainties, with negative angles denoting west-from-north polarization directions. Polarized fluxes, obtained by multiplying the total fluxes within the beams by their corresponding percentage polarizations, range from 0.22 to 2.1 Jy. The sources for which we measured upper limits to percentage polarization, W3(E), NGC 6334, and M17, have 2 σ upper limits to their polarized fluxes of 0.74, 1.5, and 1.8 Jy, respectively.

3. RESOLUTION ENHANCEMENT OF *IRAS* IMAGES

IRAS co-added survey images have angular resolutions of a few arcminutes, mostly because of the large sizes of the 60 and

TABLE 1

MILLIPOL 1300 MICRON POLARIZATION SUMMARY

Cloud Core (1)	α (1950) (2)	δ (1950) (3)	Flux (Jy) (4)	P (%) (5)	χ (6)
Sgr B2 (N)	$17^h44^m08^s.8$	−28°21'15"	37.0	0.83 ± 0.26	22° ± 9°
Sgr B2 (S)	17 44 09.2	−28 22 07	58.0	0.55 ± 0.15	−26 ± 7
W49	19 07 49.6	+09 01 24	27.0	0.94 ± 0.44	35 ± 12
W51	19 21 25.9	+14 24 34	43.5	0.50 ± 0.21	−31 ± 11
W3(W)	02 21 43.1	+61 52 45	12.0	2.09 ± 0.98	−34 ± 13
DR 21	20 37 14.5	+42 09 15	27.0	4.47 ± 1.10	15 ± 7
OMC-1	05 32 46.7	−05 24 16	45.5	4.60 ± 0.43[a]	31 ± 11[a]
W3(E)	02 21 57.1	+61 52 33	12.0	6.15[b]	...
NGC 6334	17 17 33.0	−35 44 00	25.0	5.95[b]	...
M17	18 17 29.8	−16 12 51	22.0	8.16[b]	...

[a] Average of 15 positions (see Leach et al. 1991).
[b] 2 σ upper limit.

100 μm detectors and because of the scanning motion of the satellite and coarse sampling of the detected signal. In contrast, the half-power beamwidth at $\lambda = 1300$ μm of the NRAO 12 m telescope is 30″. Thus, the *IRAS* survey angular resolution required enhancement by at least a factor of 2 to facilitate a comparison between the MILLIPOL results and the *IRAS* images. We elected to enhance the resolution of the *IRAS* images through direct Fourier deconvolution of the blurring effect of the observed point spread function (PSF) in each image. This method is computationally accurate and reasonably effective for our purposes.

We first median-filtered each raw 1° × 1° *IRAS* co-added image (241 × 241 pixels) with a large kernel (greater than 17′) to remove large-scale background variations. The smoothed image was then subtracted from the original to enhance small-scale variations. The four band images (12, 25, 60, and 100 μm) were examined and candidate PSFs were identified based on three criteria: the existence of a bona fide point source at $\lambda = 12$ μm (as compared to other point sources in the 12 μm images); good signal-to-noise in all four bands; and distinct spatial separation from both diffuse emission *and* the MILLIPOL target source in those bands. Using IRAF,[1] an average PSF was created from all viable PSF candidates in each field for each of the 60 and 100 μm images. These average PSFs were constructed by normalizing individual PSFs to unit-integral values and averaging. The average PSF for each image was smoothed with a narrow circular Gaussian (typically $\sigma \leq 1$ pixel), so that ringing effects, typically seen in Fourier deconvolution of objects with sharp edges, were minimized. The *IRAS* median-cleaned image and the PSF were then Fourier-transformed using a two-dimensional FFT algorithm. The transform of the PSF was subsequently divided into the transform of the *IRAS* median-cleaned image, and the resultant image was inverse-transformed back into the image plane. The preceding steps introduced high spatial-frequency noise, so the deconvolved images were smoothed by convolving with circular Gaussians. The full widths at half-maximum of the convolving Gaussians were selected to be as narrow as the minor axes of the ellipses characterizing the average PSFs, typically ∼1.′3.

Figures 1–3 show portions of the *IRAS* images before enhancement, the point spread function used in the enhancement process, and the corresponding image after enhancement, respectively, for Orion (OMC-1) at $\lambda = 60$ μm. Figure 1 shows contours of 60 μm emission toward OMC-1 after the image had been median-cleaned to remove the largest scale background variations. The peak intensity is 15,559 MJy sr^{-1}, and the root mean square noise away from the source is 26 MJy sr^{-1}, for a peak signal-to-noise ratio of ∼600 to 1. This unenhanced image of OMC-1 is dominated by a strong central blob of emission, whose angular size (FWHM) is ∼6′. Figure 2 shows the PSF obtained from the 60 μm intensity map of OMC-1 using the method described above. The angular size (FWHM) along the narrowest direction is ∼1.′5. Figure 3 shows the same portion of the sky as Figure 1, after the median-cleaned *IRAS* image had been processed by deconvolving the effective PSF and subsequently smoothing with a 1.′25 (FWHM) circular Gaussian beam. The peak intensity is 18562 MJy sr^{-1}, and the root mean square noise away from the source is 39 MJy sr^{-1}, for a peak signal-to-noise ratio of ∼500 to 1. The appearance of approximately eight separate emission peaks suggests an effective angular resolution of ∼2′. Thus the enhancement process has increased the angular resolution of the *IRAS* image by a factor of 2–3.

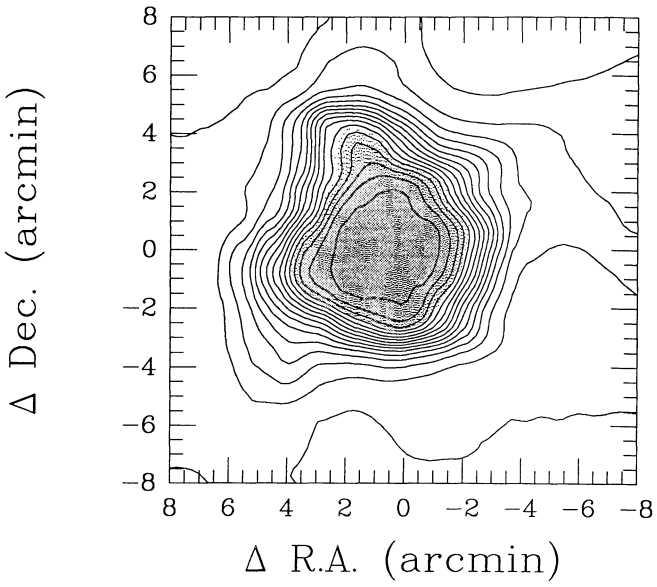

FIG. 1.—Contour map of the 60 μm intensity of OMC-1 in MJy sr^{-1}, from 0 to 15000, in steps of 1000. The image had been cleaned with a median filter.

Using the enhanced 60 and 100 μm images, dust color temperature and opacity maps were computed for each source, using a single temperature, modified blackbody model (see Clemens, Yun, & Heyer 1991). Figures 4–9 show contours of 100 μm optical depth, as determined from the enhanced resolution 60 and 100 μm *IRAS* images, for each source. The dashed circle indicates the size (FWHM) of the *larger* of the two restoring circular Gaussian beams for the 60 and 100 μm intensity images used to create each opacity image. The figures

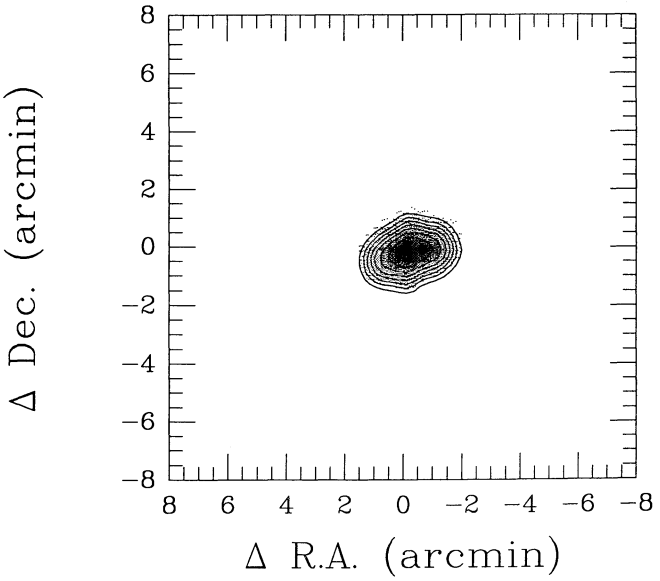

[1] IRAF is distributed by National Optical Astronomy Observatories, which are operated by the Association of Universities for Research in Astronomy, Inc., under contract with the National Science Foundation.

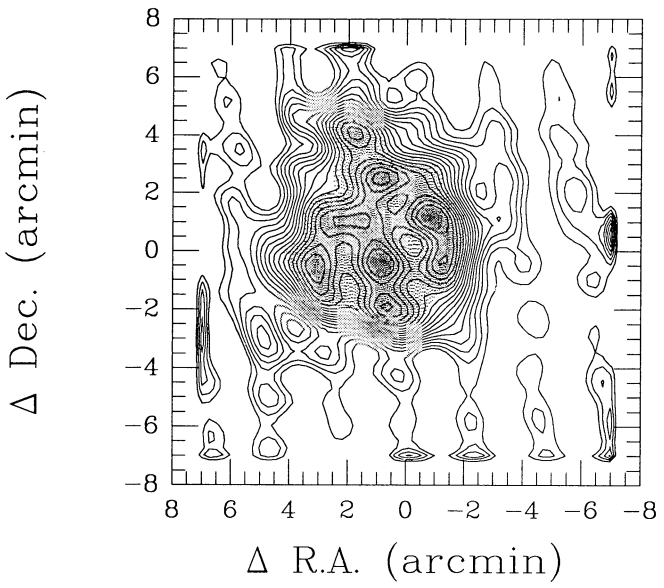

FIG. 3.—Contour map of the 60 μm intensity of OMC-1 in MJy sr^{-1}, from 1000 to 18,000, in steps of 1000. The image is a Fourier deconvolution of the PSF (Fig. 2) from the unenhanced intensity image of OMC-1 (Fig. 1).

are also overlaid with the beam size and polarization direction of the MILLIPOL measurement, and with observed bipolar outflow directions. Some features in these images are noise artifacts due to both deconvolution of the intensity images and the subsequent use of the single-temperature model, especially where negative intensity pixels resulted in discontinuities in the temperature and opacity images. There was some uncertainty in the registration of the *IRAS* coordinate system relative to that of MILLIPOL. *IRAS* point source positional uncertainties have typically been quoted as ranging from a few arcseconds up to as much as several arcminutes. Here, the typical offsets were ~15″–30″.

Dusty clumps in the opacity images located near the MILLIPOL target sources were assessed to characterize their peak 100 μm opacity values, positions, ratios of their major to minor axes (a/b), and position angles (χ_{IRAS}) of their major axes. The last two parameters were derived by maximizing the ratio of the long axis to the (assumed perpendicular) short axis of the half-power contour around the opacity peak. If the extent of the half-power contour was smaller than the diameter of the smoothing beam, then the nearest contour encompassing the resolution size defined by the smoothing was chosen to delineate the axis ratio and position angle of the cloud core. Table 2 lists a comparison of position angles determined from the MILLIPOL measurements of Table 1 and from measurement of enhanced *IRAS* dust opacity contours, along with the cloud core axis ratios. The MILLIPOL value listed for Sagittarius B2 is the weighted average of the values measured for the two positions observed; the *IRAS* resolution of ~1.2 prohibits separate comparison of these two positions, which are only 52″ apart. Column (3) lists the position angles measured from the contour plots of 100 μm dust opacity for the resolution-enhanced *IRAS* images. The 10° uncertainty in the cloud core major axis position angles is an average value derived using the following method: for the opacity contours of each cloud core, mutually perpendicular diameters were measured from the opacity peak to the half-power contour in either direction, at all possible azimuth angles, in steps of 5°, yielding an empirical

TABLE 2

COMPARISON OF MILLIPOL AND *IRAS* CLOUD CORE PROPERTIES

Cloud Core (1)	$\chi_{MILLIPOL}$ (2)	χ_{IRAS} (3)	$\Delta\chi$ (4)	Axis Ratio (5)	T_{dust} (K) (6)	τ_{100}(Peak) (7)
Sgr B2	−8° ± 8°[a]	12° ± 10°	20°	1.5	37	0.150
W49	35 ± 12	5 ± 10	30	2.3	47	0.010
W51	−31 ± 11	−19 ± 10	12	3.0	46	0.005
W3(W)	−34 ± 13	57 ± 10	89	2.5	43	0.008
DR 21	15 ± 7	15 ± 10	0	3.2	49	0.007
OMC-1	31 ± 11	37 ± 10	6	3.0	45	0.005

[a] Weighted average of N and S positions.

relationship between axis ratio and aximuth angle. The peak axis ratio was established, and the uncertainty in the orientation angle was estimated from the half-maximum half-width of the peak axis ratio function plotted against azimuth angle. Column (4) of Table 2 lists the acute angle between the position angles from column (3) and the polarization angles from column (2). Column (5) lists axis ratios obtained from the dust opacity contours. Colum (6) lists the 60/100 μm dust temperatures obtained from resolution-enhanced *IRAS* images, averaged over the effective beamwidth for the MILLIPOL observations. Column (7) lists the peak 100 μm dust opacity value nearest the source position coordinates listed in Table 1.

4. DISCUSSION

4.1. *Individual Sources*

This section presents a more detailed treatment of each of the sources detected using MILLIPOL. In addition to the comparison of the cloud core position angles inferred from MILLIPOL measurements and *IRAS* dust opacity maps, morphological comparisons are made to the results of other continuum, line, and molecular outflow studies.

4.1.1. *DR 21*

DR 21 is at a distance of ~2 kpc (Dickel, Wendker, & Bieritz 1969). The north-south extent of 7′ as seen in 50 and 100 μm continuum emission (Harvey et al. 1986) indicates a physical size of ~4 pc for a ridge of enhanced dust column density inside the cloud core. This ridge was also seen at $\lambda = 53$ μm with 20″ resolution at position angle 0° by Harvey, Campbell, & Hoffmann (1977, hereafter HCH). Our MILLIPOL detection indicates a polarization position angle of 15° ± 7° (Fig. 4), oriented along the longest axis of this dusty ridge (some of which appears in Fig. 4), at the position of the northernmost of four 5 GHz sources found by Harris (1973). Our optical depth map, constructed from the resolution-enhanced *IRAS* 60 and 100 μm images, has a peak $\tau_{100} = 0.007$, agreeing well with the lower limit $\tau_{90} \geq 0.005$ calculated by Campbell et al. (1982). In addition, the *IRAS* optical depth contours appear to be somewhat elongated in a direction almost identical to that of the dust ridge and the MILLIPOL polarization direction. Our 60/100 μm peak dust temperature from the enhanced *IRAS* images is 49 K, essentially identical to the 47 ± 7 K derived by HCH for the same position.

Bally & Lada (1983) discovered a bipolar molecular outflow from DR 21. It is one of the most highly collimated outflows found. This outflow has been delineated in the ^{12}CO, ^{13}CO, and C^{18}O ($J = 1$–0) rotational lines, and the H53α recombination line by Garden et al. (1991, hereafter G91); in 63 μm

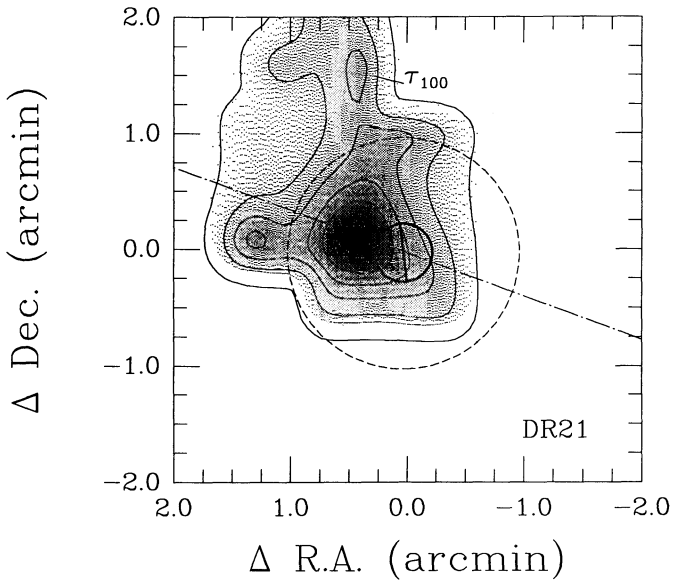

FIG. 4.—Contour map of the 100 μm opacity of the DR 21 cloud core. Contours are 1 × 10^{-4}, and 0.001 to 0.006, in steps of 0.001. The small bold circle and bar indicate the MILLIPOL beam and polarization position angle. The large dashed circle indicates the FWHM size of the larger of the two circular Gaussian beams used to smooth the deconvolved 60 and 100 μm intensity images of DR 21. The dot-dashed line indicates the direction of the principle bipolar molecular outflows seen by Lane et al. (1990) and Garden et al. (1991).

[O I], 35 μm [Si II], 158 μm [C II], and 119 μm CO (J = 22–21) by Lane et al. (1990); and in vibrationally excited molecular hydrogen line emission by Garden et al. (1986). Each study found highly collimated, bipolar molecular outflows aligned in a general east-west direction, orthogonal to the high-density dusty ridge seen in the far-infrared continuum. Lane et al. deduce that an embedded source with luminosity ~6 × 10^5 $L_\odot$ and OB spectral type was producing the jet seen in 63 μm continuum (at P.A. 70°). G91 adopted a bolometric luminosity of ~2 × 10^5 $L_\odot$, the value proposed by HCH; this luminosity is characteristic of a single O6V star. However, G91 conclude that there are at least *two other* bipolar outflows, so that the spectral types of the embedded O-star cluster members are likely to be later than O6. G91 found two outflows of hydrogen, one of which (the larger) had also been found by Bally & Lada, Lane et al., and Garden et al. (1986). Both of these outflows have position angles of ~70°.

MILLIPOL was used to detect polarized emission from the dust in the dense core of DR 21. The polarization position angle is roughly the same as the general extent of the dusty ridge (north-south) seen in the enhanced *IRAS* opacity image. Outflows from the DR 21 cloud core proceed generally perpendicularly (east-west) to this ridge.

4.1.2. *Sagittarius B2*

The giant molecular cloud Sagittarius B2 is one of the most luminous and highest hydrogen column density regions of star formation in the Galaxy. It is located within a few hundred parsecs of the Galactic center (Vogel, Genzel, & Palmer 1987, hereafter VGP) at a distance of ~7.5 kpc from the Sun. HCH derived H_2 column densities which ranged from 6 × 10^{23} to 10^{25} cm^{-2} across the cloud. These values are several orders of magnitude greater than the average for GMCs (HCH). Sagittarius B2 contains two clusters of H II regions and H_2O and OH maser sources which are separated by 45″ (~1.6 pc) along a north-south line (Benson & Johnston 1984). We have observed the 1300 μm polarization toward both of these clusters, denoted Sagittarius B2(N) and Sagittarius B2(S) in Table 1 (also see Fig. 5). GJ observed 1300 μm continuum from this region, and found that the total flux was dominated by dust emission, with a north-south extent.

Goldsmith and collaborators have made a number of millimeter and high angular resolution submillimeter and far-infrared observations of Sagittarius B2. Goldsmith, Snell, & Lis (1987) observed 1300 μm continuum emission from Sagittarius B2 and found the emission source to be elongated in a north-south direction, peaking near our MILLIPOL position Sagittarius B2(N). They found that optically thick foreground dust obscures the northern peak in the far-infrared. Goldsmith et al. (1990) found similar results at 350, 450, 850, and 1100 μm. Goldsmith et al. (1992) observed at 50 and 100 μm, and derived, with MEM deconvolution, a λ = 50 μm intensity map dominated by the source Sagittarius B2(M). Sagittarius B2(M) corresponds to our MILLIPOL position Sagittarius B2(S).

Carlstrom and Vogel (1989, hereafter CV) mapped Sagittarius B2 at λ = 3.4 mm with 5″ × 3″ resolution. Their 3.4 mm dust features coincide well with features seen in continuum at λ = 1.3 cm and in various ammonia inversion transitions as mapped by VGP. CV also provided a detailed look at Sagittarius B2(N) in the 3.4 mm continuum dust emission; structures in the dust were resolved down to 1″ (0.04 pc). Two elongated dusty clumps straddle the northern H_2O maser sources at a position angle of 20°; each has a rough north-south extent. Our MILLIPOL results (P.A. = 22° ± 9°) for Sagittarius B2(N) are consistent with the orientations of 3.4 mm emission features seen by CV. HCH produced a dust temperature map from a comparison of 20″ resolution 53 μm brightness temperature and a blackbody three-color temperature fit to their 53 μm and 30″ resolution 100 and 175 μm

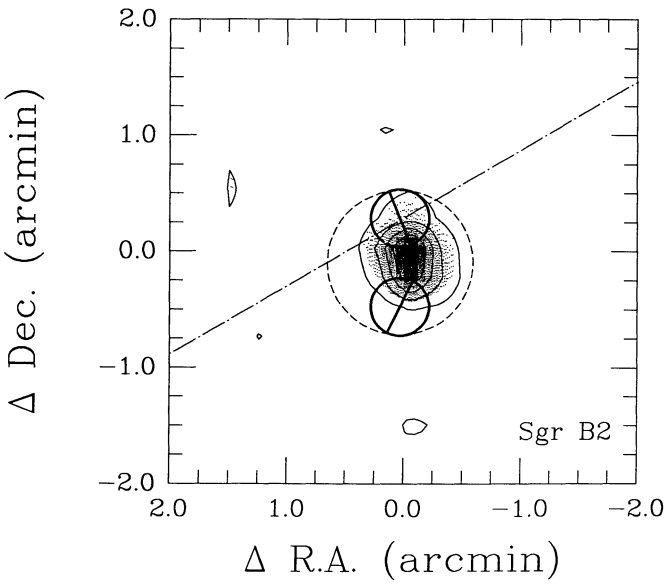

FIG. 5.—Contour map of the 100 μm opacity of Sgr B2, from 0 to 0.15, in steps of 0.025. The small bold circles and bars indicate the MILLIPOL beams and polarization position angles. The large dashed circle indicates the FWHM size of the larger of the two circular Gaussian beams used to smooth the deconvolved intensity images of Sgr B2. The dot-dashed line indicates the direction of the bipolar CO outflow seen by Vogel et al. (1987).

data. They derived a dust temperature of 33 K for the position corresponding to Sagittarius B2(N). Our *IRAS* resolution-enhanced temperature map (1'.25 resolution) suggests a warmer dust temperature of 37 K at that same position.

Our observations of Sagittarius B2(S) were centered on the ultracompact H II region E, in the nomenclature of Benson & Johnston (1984). Their $\lambda = 2$ cm continuum map shows emission dominated by the slightly larger compact region F, $\sim 5''$ (0.2 pc) to the north of E. Both F and E have long axes oriented at P.A. $= -20°$, and other nearby ultracompact H II regions show similar alignments. Our MILLIPOL polarimetry yielded a position angle of $-26° \pm 7°$.

Churchwell et al. (1986) concluded that there are two dust temperature populations. Analysis of their observations of HNCO, which is radiatively excited by dust-emitting radiation primarily between the wavelengths of 100 and 300 μm, suggested that the peak 100 μm dust opacity was ~ 0.3, exceedingly high for a GMC. Our dust opacity maps constructed from *IRAS* images yield $\tau_{100} = 0.15$, which is ~ 100 times higher than the opacities for our other MILLIPOL-detected GMC cores.

There is no evidence of collimated outflows in Sagittarius B2(N) or (S), but VGP detected a rather diffuse bipolar outflow in NH_3 originating from the northern source. Other indications of outflows (such as the mass-loss rate of $10^{-2}\ M_\odot$ year^{-1} inferred by CV) support the idea of energetic but more isotropic outflows than those seen in other GMC cores. The apparent isotropy may be due to a viewing direction along the outflow axis, but there is insufficient evidence to draw a firm conclusion.

MILLIPOL was used to detect polarized emission from the dust in Sagittarius B2 with a polarization position angle close to the general extent of the dust (north-south) seen in the enhanced *IRAS* opacity image. Outflows from Sagittarius B2 appear isotropic, but this may be a viewing effect; the line connecting the peaks of blue- and redshifted emission of the ammonia (VGP) has a position angle roughly perpendicular to the dust ridges and MILLIPOL polarization position angles.

4.1.3. *W3*

The W3 star-formation complex lies in the Perseus spiral arm ~ 3 kpc from the Sun (Bieging, Wilson, & Downes 1982), on one edge of the enormous H II region W4. The $\lambda = 1$ mm continuum map of Westbrook et al. (1976), with an angular resolution of 1', shows a dusty structure extending in a generally east-west direction with an apparent size of 3' (2.6 pc). Their map contours trace the positions of near-infrared sources and compact H II regions, whose distribution suggests two separate clumps of high-density gas, one centered near IRS 5 in the eastern part of W3, the other centered $\sim 20''$ south of IRS 4. A study of the velocity field in the core (Hayashi et al. 1989) supported the scenario of two dust ridges with different orientations. Our MILLIPOL observations examined these peaks individually (Table 1); only the western peak near IRS 4 produced a 2 σ detection in the 1300 μm polarized continuum (Fig. 6). We derive a polarization position angle of $-34° \pm 13°$, which is the general direction suggested by the 1 mm flux density distribution of Westbrook et al. and by the 400 μm emission distribution of Jaffe et al. (1983). GJ noticed that the eastern source is brighter at $\lambda = 50$ μm (Werner et al. 1980) than at 1.3 mm, while the reverse is true of the western source. GJ conclude that the eastern source lies in front of its associated H II region, while the western source lies behind its H II region.

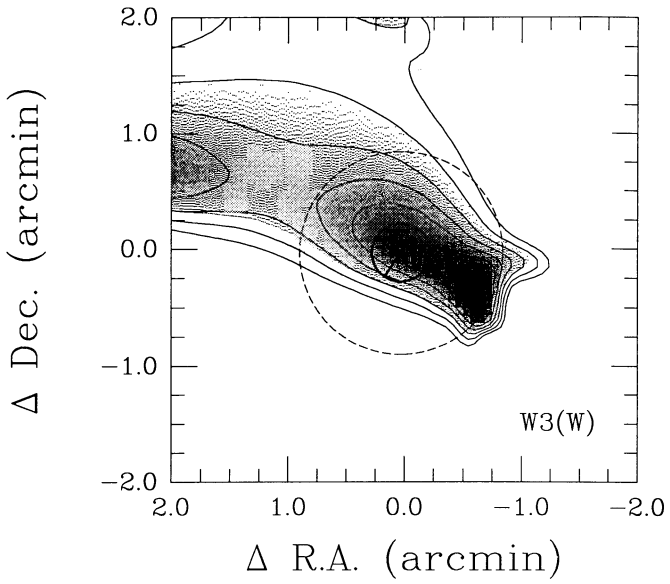

FIG. 6.—Contour map of the 100 μm opacity of W3(W), from 0.003 to 0.008, in steps of 0.001. The small bold circle and bar indicate the MILLIPOL beam and polarization position angle. The large dashed circle indicates the FWHM size of the larger of the two circular Gaussian beams used to smooth the deconvolved intensity images of W3(W).

P91 found similar polarimetric results in the far-infrared. Their position 3 closely corresponded to our nondetected MILLIPOL position W3(E), and they set an upper limit of $\sim 1\%$ polarization for that position. Similarly, their position 5 most closely matches our MILLIPOL position W3(W); their detected percentage polarization and position angle are in agreement with our MILLIPOL values.

Arnal et al. (1982) mapped $\lambda = 6$ cm continuum and H_2CO absorption with $\sim 9''$ resolution. Their continuum map shows the two westernmost sources (diameters 0.2 and 0.4 pc; our beam covered both) connected by emission whose long axis matches well with the position angle we derived using MILLIPOL. On the other hand, our enhanced resolution *IRAS* images produce opacity maps whose contours suggest a cloud core position angle nearly orthogonal to the MILLIPOL polarization angle.

Dickel et al. (1980) provided extensive observations of CO, CS, and HCN, which indicated that W3 is undergoing collapse. Their map of CO emission shows part of an extensive shell extending more than 15 pc from northeast to southwest. Thronson, Lada, & Hewagama (1985) suggested that this CO emission is part of the ionization front of the contiguous H II region W4, which has evolved to a diameter of 60 pc. The same CO map of Dickel et al. shows smaller CO features extending from southeast to northwest, possibly due to bipolar outflows from the sources IRS 5, 6, and 7. Thronson (1986) found a blueshifted CO lobe extending northward from these sources, but could not determine the source, and did not find any corresponding redshifted lobe. In contrast, Claussen et al. (1984) found clear evidence of blue- and redshifted CO lobes with an apparent east-west separation of only 2".5, centered upon IRS 5. The alignment of the CO outflow with the dusty emission around IRS 5 and the other eastern sources suggests that we are observing gas and dust being swept up in the far side of the W4 ionization front, which appears nearly edge-on at the position of W3(E) (Dickel et al.; Thronson et al. 1985). However, W3(W) does not yet appear to have been affected by the ioniza-

tion front. Dust destruction due to ionizing radiation or a shock might explain why emission toward W3(E) does not appear significantly polarized. Emission toward W3(W) is polarized at the 1%–2% level (P91; Table 1), and toward W3(W) there is dusty emission nearly orthogonal to that around W3(E), but there is no evidence of outflows from IRS 4.

MILLIPOL was used to observe two positions toward the W3 cloud core, and polarized emission was detected with 2 σ certainty toward the western position. The polarization position angle toward W3(W) is nearly orthogonal to the dusty ridge seen in the enhanced *IRAS* opacity image. No energetic, collimated outflows are known toward W3(W).

4.1.4. *W49*

Among the cloud cores in GMCs studied in this survey, W49 is probably the most distant, at 11 kpc from the Sun (SSS; Gwinn et al. 1989), and 7.5 kpc from the Galactic center. SSS mapped the 1300 μm continuum emission of W49 and found that it arises from a compact source of angular size less than 45″, which coincides with the location of peak far-infrared emission mapped by HCH. On the HCH 53 μm continuum map, there is a long ridge of emission extending northeast to southwest for $\sim$3′ (9 pc) with an orientation angle of $\sim$35°; our polarization position angle, derived from MILLIPOL data obtained toward the far-infrared peak, is in close agreement at 35° $\pm$ 12° (Fig. 7). GJ observed the 1300 μm continuum of W49 and noted that the far-infrared peak seen by HCH was offset from the millimeter wavelength peak by $\sim$30″, about one beamwidth in each study.

Dickel & Goss (1990) mapped the 2 cm continuum emission with the VLA at a resolution of 2″ (0.1 pc), finding a number of ultracompact H II regions. Our observed position covers the ultracompact region F (following their nomenclature). W49 North-F is one of four, perhaps five, 0.1 pc diameter H II regions stretching across 1 pc along a position angle of $\sim$40°. This association of UC H II regions appears to be the northern arc of a ring of H II regions (Welch et al. 1987).

Scoville et al. (1986) discovered a bipolar CO outflow emanating from the UC H II complex W49 North-G, 10″ southeast of W49 North-F. The blueshifted and redshifted emission peaks are separated by 5″ (0.3 pc) along a position angle of about $-$65° (see their Fig. 8, and our Fig. 7), which is orthogonal to the plane of dust emission and MILLIPOL polarization. Dickel & Goss (1990) argued for a model of a diffuse cloud collapsing onto a rotating high-density molecular disk to explain the configuration of the ring of H II regions and their peculiar velocity features, and the lobes of CO outflows from W49 North-G. Their evidence points to a situation where the disk is inclined with respect to the plane of the sky and with respect to the line of sight.

MILLIPOL was used to make a 2 σ detection of the polarized emission of dust in W49, and the polarization position angle was roughly the same as the extent of the dust ridge seen in the enhanced *IRAS* opacity image. There is evidence of outflow perpendicular to this dust ridge.

4.1.5. *W51*

W51 is an extremely large complex of H II regions $\sim$7.5 kpc from the Sun. Martin (1972) first resolved the bright, extended H II region W51 (G49.5–0.4) into numerous components, of which two of the more luminous sources, IRS 1 and IRS 2 (Wynn-Williams et al. 1974), are connected by a ridge of emission extending $\sim$1′.5 (3 pc) to the northwest from IRS 1, which is also called W51e. SSS mapped the 1300 μm continuum from W51e and IRS 2, and found them to be of roughly equal intensity. Thronson & Harper (1979) mapped the λ = 74 μm continuum with a 30″ beam. Their map shows a distinct ridge extending along P.A. $-$30°. GJ compared their 1300 μm emission contours with the far-infrared map of Thronson & Harper, and, like SSS, found two 1300 μm intensity peaks. However, GJ found one peak is weaker and corresponds to the far-infrared emission peak.

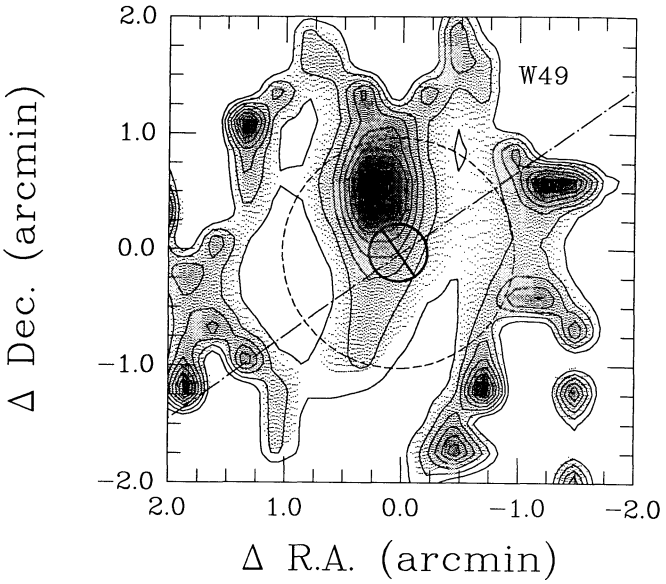

FIG. 7.—Contour map of the 100 μm opacity of W49, from 0.002 to 0.01, in steps of 0.001. The small bold circle and bar indicated the MILLIPOL beam and polarization position angle. The large dashed circle indicates the FWHM size of the larger of the two circular Gaussian beams used to smooth the deconvolved intensity images of W49. The dot-dashed line indicates the direction of the bipolar CO outflow seen by Scoville et al. (1986).

Our polarimetry was confined to the ultracompact source W51e1 discovered by Turner et al. (1974), near the OH maser location W51 South (Raymond & Eliasson 1969). A 2 cm continuum map by Kogut et al. (1989) showed the diameter of W51e1 to be $\sim$5″ (0.2 pc). We derive a polarization position angle of $-$31 $\pm$ 11° (Fig. 8). This value agrees well with the position angle of the structure seen in the map of Thronson and Harper, and with the direction of the long axis of the opacity peak in our *IRAS* map. P91 mapped six positions toward W51 using λ = 100 μm polarimetry. Their position 2 is nearest our MILLIPOL position, and they derived a percentage polarization and a position angle very similar to our values.

In their high-resolution study of warm NH_3 near the maser sources in IRS 1 and IRS 2, Ho, Genzel, & Das (1983) summarized indications of the presence of an energetic molecular outflow and of its interaction with enhanced-density material. The ammonia emission was found to have a north-south extent roughly parallel to our *IRAS* 100 μm dust opacity contours.

MILLIPOL was used to make a 2 σ detection of the polarized emission from dust in the core of W51, at a polarization position angle very close to the orientation angle of the dust ridge seen in the enhanced *IRAS* opacity image. Evidence of outflows so far indicates that they are oriented parallel to the dust ridge.

4.1.6. *OMC-1*

The full details of the MILLIPOL polarimetric study of Orion are contained in L91. Because of the proximity and 1300

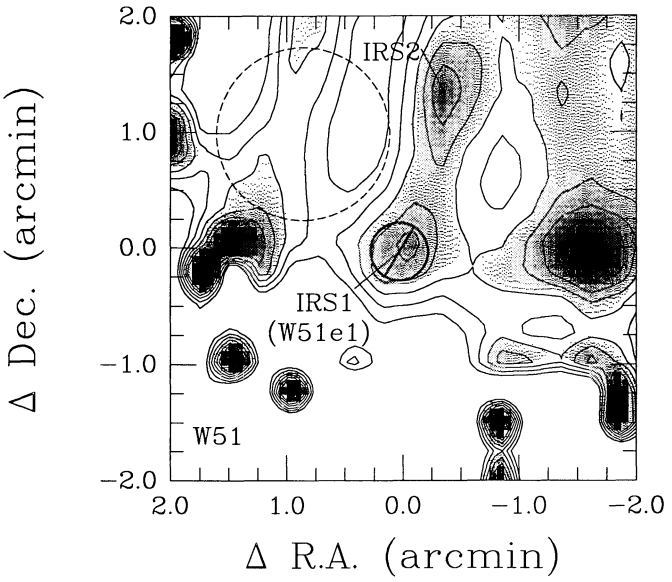

FIG. 8.—Contour map of the 100 μm opacity of W51, from 0.002 to 0.0045, in steps of 0.005. The small bold circle and bar indicate the MILLIPOL beam and polarization position angle. The large dashed circle indicates the FWHM size of the larger of the two circular Gaussian beams used to smooth the deconvolved intensity images of W51. Source nomenclature follows Wynn-Williams et al. (1974) and Turner et al. (1974).

μm brightness of OMC-1, a polarization map was able to be constructed. The major findings of that study were

1. The polarization position angles were remarkably uniform over the entire 0.3 pc region, and the angular dispersion was quite small, suggesting that there is a large-scale uniform magnetic field which could be quite strong (perhaps ~1 mG) (G90; L91). The MILLIPOL average polarization P.A. is 31° ± 11° (see Fig. 9).

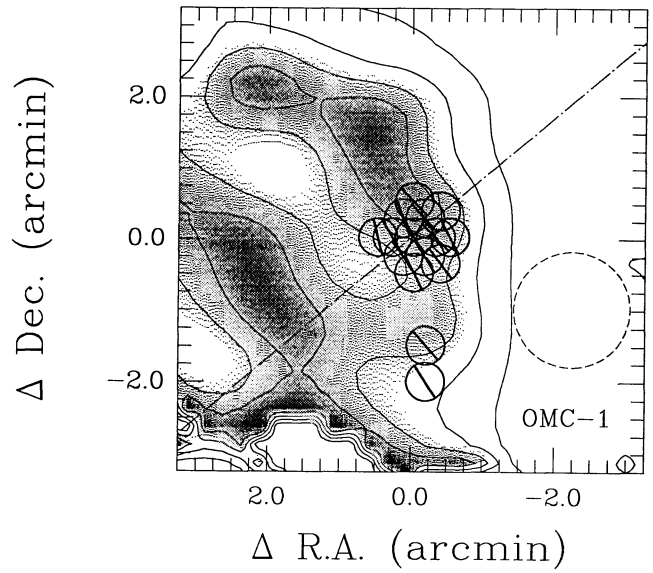

FIG. 9.—Contour map of the 100 μm opacity of OMC-1, from 0 to 0.004, in steps of 0.001. The small bold circles and bars indicate the MILLIPOL beams and polarization position angles. The large dashed circle indicates the FWHM size of the larger of the two circular Gaussian beams used to smooth the deconvolved intensity images of OMC-1. The dot-dashed line indicates the direction of the CO outflow discovered by Erickson et al. (1982).

2. The average polarization is 4.6%, increasing outward from BN/KL. Our favored explanation for the polarization dip toward the center of OMC-1 combines a change in the line of sight orientation of the magnetic field with field line tangling.

Burton et al. (1991, hereafter B91) mapped the polarization of the molecular hydrogen vibrational line emission at $\lambda = 2.12$ μm with an angular resolution exceeding 1″. Polarization in the near infrared is due to preferential *absorption* by magnetically aligned dust grains (Davis & Greenstein 1951) and to scattering from optically thick regions. Therefore we might expect to see some polarization vectors perpendicular to those seen via dust *emission* at millimeter and submillimeter wavelengths. Accordingly, the map of B91 shows coherence in the orientation of polarization position angles very near BN/KL (at $\chi = -55°$), but orthogonal to those found at $\lambda = 1300$ μm. Notably, they find that there is a decrease in the percentage polarization near BN/KL (from 7% to 4%); they too adopt a twisted field scenario to explain their results. They also note that the core vectors align well with the CO outflow emanating from the central source IRc2. Interestingly, B91 find that the ordered field region ends near the Herbig-Haro object M42-HH 1 located ~50″ from BN/KL, whereupon the centrosymmetric pattern of polarization vectors implies scattering by an H_2 reflection nebula (an optically thick background screen).

MILLIPOL was used to detect polarized emission from dust toward the core of OMC-1 at 15 different positions. The very similar polarization position angles indicate that there is a large-scale uniform component to the magnetic field, and the polarization is aligned with the dust ridges seen in the enhanced *IRAS* opacity images. An outflow from IRc2 is oriented perpendicular to these dust ridges.

4.2. *Correlation of Dust Structures with Magnetic Field Directions*

In this section, the morphologies of the cloud core regions seen in the enhanced *IRAS* opacity images are compared with the magnetic field properties deduced from the MILLIPOL observations. Correlations were sought between opacity, temperature, detection rate, ellipticity, and position angle differences.

Figure 10 displays the cumulative fraction of sources with detected (and undetected) MILLIPOL polarizations as a function of their enhanced *IRAS* peak 100 μm opacities. From the figure, we conclude that more opaque cloud core sources are more likely to emit detectable polarized radiation at millimeter wavelengths (which may represent only a manifestation of a flux limit in an optically thin regime). The figure also indicates that dust, the source of the opacity, is also the source of the linearly polarized emission.

Figure 11 displays the cumulative fraction of MILLIPOL detections and nondetections as functions of the enhanced *IRAS* peak 60/100 μm dust temperature. The figure indicates that the cooler sources were more likely detected using MILLIPOL. However, the single-temperature blackbody model used (Clemens, Yun, & Heyer 1991) tends to correlate low temperatures with high opacities, and could be used to *predict* Figure 11 from Figure 10. Nevertheless, this figure and Figure 10 indicate that magnetic fields are easier to detect in molecular cloud cores which have not yet become significantly heated or perturbed by massive star formation.

Figure 12 displays the histogram of the absolute value of the acute angle between the position angle of the long axis of the

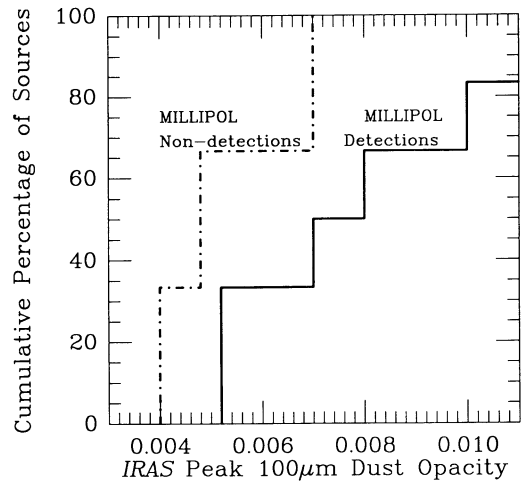

FIG. 10.—Cumulative fraction of MILLIPOL-detected and non-detected sources as a function of *IRAS* peak 100 μm dust opacity.

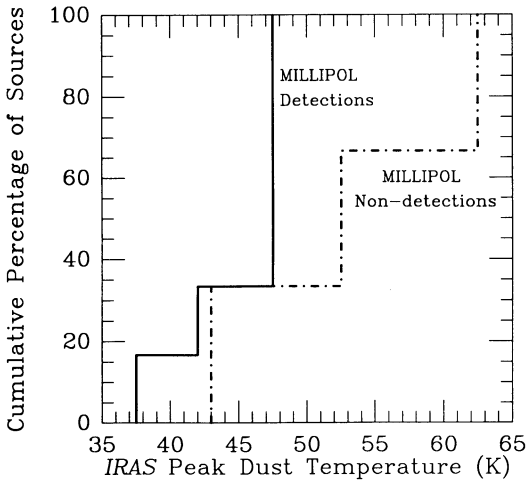

FIG. 11.—Cumulative fraction of MILLIPOL-detected and nondetected sources as a function of *IRAS* peak dust temperature.

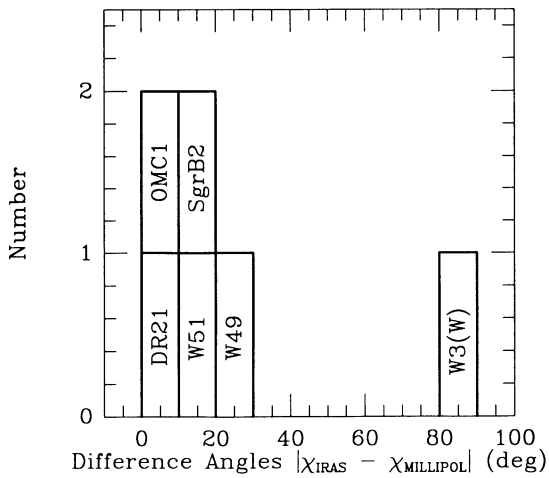

FIG. 12.—Histogram of difference angles between MILLIPOL polarization angles and *IRAS* cloud-core major-axis position angles.

dust structure and the MILLIPOL polarization position angle, for the detected cloud cores. There is a strong probability of alignment, as indicated by the bunching of sources near 0°. There is one source [W3(W)] which exhibits orthogonality instead of alignment. If all the detected sources are considered and the signed differences between the magnetic field and dust position angles are considered, the mean acute position angle difference is −14°, with a dispersion of 34°. However, if W3(W) is excluded, the mean position angle difference of the remaining sample is −2°.2, with a dispersion of 17°, and a mean error of the mean of 5°, comparable to the uncertainties in either the MILLIPOL or *IRAS* angles.

Whereas Figure 10 shows that more opaque sources are more likely to be detected by MILLIPOL as sources of polarized dust emission, Figure 13 shows that the MILLIPOL *percentage* polarization is not strongly correlated with the 100 μm opacity. The large uncertainties in percentage polarization lead to a 63% chance that the decreasing trend seen visually in the data is due to random sampling.

Figure 14 displays the similar MILLIPOL percentage polarization versus *IRAS* peak dust temperature. As for the case of the dust opacity, it is unlikely that percentage polarization is related to dust temperature.

One interesting correlation is shown in Figure 15. There, the ratio of major to minor axes of the dust in the cloud cores, as traced by the enhanced *IRAS* images, is plotted versus the alignment of the core axes with the implied magnetic field direction. Excluding the anomalous W3(W), a decreasing trend in the alignment angle with increasing axis ratio is readily apparent. The best-fit line to the remaining five points has a slope of −12° per unit change in axis ratio and has intercepts at axis ratio 3.7 for perfect alignment ($\Delta\chi = 0°$), and at alignment angle 45° for perfect cloud core sphericity (axis ratio = 1). The latter is exactly the value expected for spherical cloud cores. A linear correlation of the remaining five cloud cores yields only a 22% probability that this effect is due to chance.

4.3. *Outflow Directions and Magnetic Field Directions*

When the bipolar outflows for DR 21, OMC-1, Sagittarius B2(N), and W49 are overlaid with MILLIPOL beams and

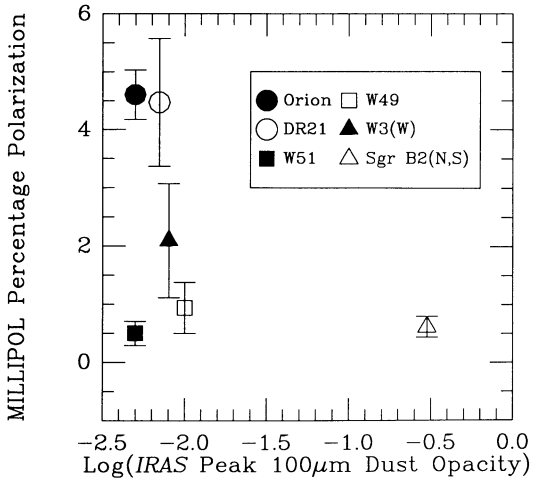

FIG. 13.—MILLIPOL percentage polarizations vs. logarithms of *IRAS* peak 100 μm opacities. The MILLIPOL polarization values for Sgr B2(N) and Sgr B2(S) have been averaged. The error for Orion is the error of the mean for 15 positions.

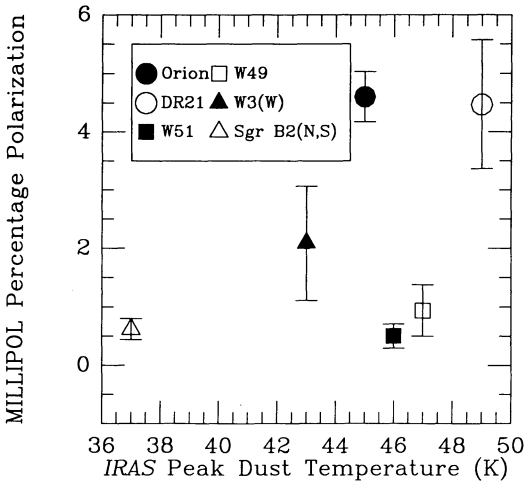

FIG. 14.—MILLIPOL percentage polarizations vs. *IRAS* peak dust temperatures. Error bars are 1 σ. Error for Orion is the error of the mean.

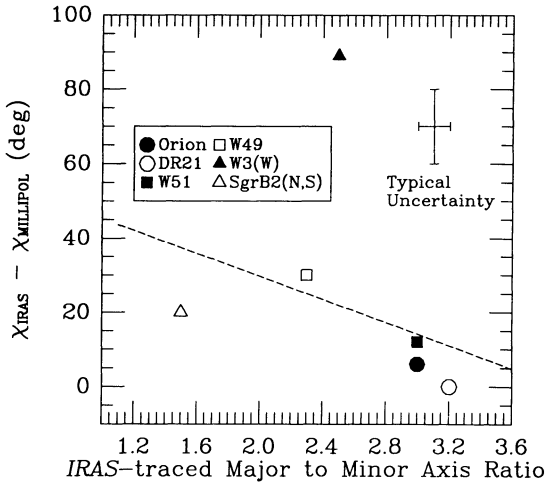

FIG. 15.—Alignment angles between MILLIPOL polarization angles and *IRAS* cloud-core major-axis position angles vs. the *IRAS*-traced major-to-minor axis ratios. The displayed error bars reflect typical uncertainties for all cloud cores. The dashed line indicates the best fit to the data sample, excluding W3(W). The slope of this line is about $-15°$ per unit change in axis ratio. The y-intercept of this line corresponds to an axis ratio of 3.7. Similarly, an axis ratio of 1 (spherical cloud) would correspond to an alignment angle of $\sim 45°$. The MILLIPOL polarization angles for Sgr B2(N) and Sgr B2(S) have been averaged.

polarizations, three of four sources show outflows along their MILLIPOL-implied magnetic field lines (see Figs. 4, 5, 7, and 9). Erickson et al. (1982) found a bipolar outflow in the CO ($J = 3$–2) line emission emanating from Orion BN/KL at a position angle of about $-60°$, orthogonal to the average MILLIPOL polarization position angle of $\sim 30°$. The implied magnetic field appears to collimate the outflow from BN/KL in the direction of the field lines. VGP detected a bipolar outflow in the NH_3 (3, 2) line from Sagittarius B2(N). The line connecting the blue- and redshifted peaks of this rather isotropic outflow has a position angle of about $-70°$, roughly orthogonal to the MILLIPOL polarization position angle of 20°. Scoville et al. (1986) found a bipolar outflow in CO ($J = 1$–0) from W49, with a position angle of $-65°$, orthogonal to the MILLIPOL polarization position angle of $\sim 35°$.

In the case of DR 21, it should be noted that G91 discovered at least three outflows in this cloud, not all colinear. Our MILLIPOL polarization direction for DR 21 likely reflects the combined effects of the magnetic fields and dust clouds around these three outflows. G91 mapped two outflows with position angles around 70°, and a third with a position angle of $-20°$, while the MILLIPOL polarization position angle is between these, at 7°.

Comparing these outflow directions with dust polarization directions indicates that the magnetic field may indeed be instrumental in directing, generating, or collimating the outflows from regions of star formation (see Blandford & Payne 1982; Draine 1983; Cohen, Rowland, & Blair 1984; Uchida & Shibata 1985; Pudritz & Norman 1986; Mundt et al. 1990).

5. SUMMARY

The first detections of linearly polarized millimeter wavelength emission from the cores of the massive star-forming regions DR 21, Sagittarius B2, W3(W) (2 σ), W49 (2 σ), and W51 (2 σ) are reported. Upper limits are reported for M17, NGC 6334, and W3(E). We have also developed a method of enhancing the angular resolution of *IRAS* images of these regions by direct Fourier deconvolution. From the enhanced *IRAS* images, we constructed dust opacity and temperature maps for these cloud cores. These two data sets were used to test for correlations between polarization directions and cloud shapes, opacities, and temperatures. We have established the following:

1. There is a strong preference for large-scale alignment between the *IRAS*-traced dust structures and the corresponding MILLIPOL-detected polarized emissions. The sense of the correlation is that the inferred magnetic field directions are generally parallel to the short axes of the elongated dust structures. The distribution of position angle differences in a sample including W3(W) has a mean of $-14°$ and a dispersion of 34°. Excluding W3(W) from the sample leads to a distribution with a mean of $-2°.2$, a dispersion of 17°, and a mean error of the mean of 5°, indicating a high degree of alignment.
2. Cloud cores which are more opaque at $\lambda = 100$ μm are more likely to have detectable polarized millimeter-wave dust emission. This confirms the known source of the opacity, dust, as the source of the polarized emission. Also, cloud cores which are cooler are more likely to have detectable polarized millimeter-wave emission.
3. Energetic outflows from these cores appear to be oriented along the directions of the magnetic fields implied by the MILLIPOL-traced polarizations.
4. The axis ratios of the *IRAS*-traced dust structures in the cloud cores in our sample are correlated with the difference between the dust polarization angles and the position angles of the long axis of the cloud.

This effort has been partially supported by NASA grant NAG 5-1160 to D. P. C. In addition, we would like to thank the anonymous referee for helpful suggestions.

REFERENCES

Aitken, D. K., Roche, P. F., Bailey, J. A., Briggs, G. P., Hough, J. H., & Thomas, J. A. 1986, MNRAS, 218, 363
Arnal, E. M., Goss, W. M., Dickel, H. R., & Forster, J. R. 1982, MNRAS, 201, 317
Bally, J., & Lada, C. J. 1983, ApJ, 265, 824
Barvainis, R., Clemens, D. P., & Leach, R. 1988, AJ, 95, 510 (BCL)
Benson, J. M., & Johnston, K. J. 1984, ApJ, 277, 181
Bieging, J. H., Wilson, T. L., & Downes, D. 1982, A&AS, 49, 607
Blandford, R. D., & Payne, D. G. 1982, MNRAS, 199, 883
Burton, M. G., Minchin, N. R., Hough, J. H., Axon, D. J., & Bailey, J. A. 1991, ApJ, 375, 611 (B91)
Campbell, M. F., Hoffmann, W. F., Thronson, H. A., Niles, D., Nawfel, R., & Hawrylycz, M. 1982, ApJ, 261, 550
Carlstrom, J. E., & Vogel, S. N. 1989, ApJ, 337, 408 (CV)
Chini, R., Kreysa, E., Mezger, P. G., & Gemünd, H.-P. 1986a, A&A, 154, L8
———. 1986b, A&A, 157, L1
Chini, R., Krügel, E., & Kreysa, E. 1986c, A&A, 167, 315
Churchwell, E., Wood, D., Myers, P. C., & Myers, R. V. 1986, ApJ, 305, 405
Claussen, M. J., et al. 1984, ApJ, 285, L83
Clemens, D. P., Leach, R. W., Barvainis, R., & Kane, B. D. 1990, PASP, 102, 1064 (C90)
Clemens, D. P., Yun, J. L., & Heyer, M. H. 1991, ApJS, 75, 877
Cohen, R. J., Rowland, P. R., & Blair, M. M. 1984, MNRAS, 210, 425
Cudlip, W., Furniss, I., King, J., & Jennings, R. E. 1982, MNRAS, 200, 1169
Davis, L., & Greenstein, J. L. 1951, ApJ, 114, 206
Dickel, H. R., Dickel, J. R., Wilson, W. J., & Werner, M. W. 1980, ApJ, 237, 711
Dickel, H. R., & Goss, W. M. 1990, ApJ, 351, 189
Dickel, H. R., Wendker, H. J., & Bieritz, J. H. 1969, A&A, 1, 270
Dragovan, M. 1986, ApJ, 308, 270
Draine, B. T. 1983, ApJ, 270, 519
Erickson, N. R., Goldsmith, P. F., Snell, R. L., Berson, R. L., Huguenin, G. R., Ulich, B. L., & Lada, C. J. 1982, ApJ, 261, L103
Garden, R., Geballe, T. R., Gatley, I., & Nadeau, D. 1986, MNRAS, 220, 203
———. 1991, ApJ, 366, 474 (G91)
Goldsmith, P. F., Snell, R. L., & Lis, D. C. 1987, ApJ, 313, L5
Goldsmith, P. F., Lis, D. C., Hills, R., & Lasenby, J. 1990, ApJ, 350, 186
Goldsmith, P. F., Lis, D. C., Lester, D. F., & Harvey, P. M. 1992, ApJ, 389, 338
Gonatas, D. P., et al. 1990, ApJ, 357, 132 (G90)
Gordon, M. A., & Jewell, P. R. 1987, ApJ, 323, 766 (GJ)
Gordon, M. A., Jewell, P. R., Kaftan-Kassim, M. A., & Salter, C. J. 1986, ApJ, 308, 288
Gwinn, C. R., Moran, J. M., Reid, M. J., Schneps, M. H., Genzel, R., & Downes, D. 1989, in IAU Symp. 136, Galactic Center, ed. M. R. Morris (Dordrecht: Kluwer), 47
Harris, S. 1973, MNRAS, 162, 5P
Harvey, P. M., Campbell, M. F., & Hoffmann, W. F. 1977, ApJ, 211, 786 (HCH)
Harvey, P. M., Joy, M., Lester, D. F., & Wilking, B. A. 1986, ApJ, 300, 737
Hayashi, M., Kobayashi, H., & Hasegawa, T. 1989, ApJ, 340, 298
Heiles, C. 1988, ApJ, 324, 321
Hildebrand, R. H. 1988, QJRAS, 29, 327
Hildebrand, R. H., Dragovan, M., & Novak, G. 1984, ApJ, 284, L51
Ho, P. T. P., Genzel, R., & Das, A. 1983, ApJ, 266, 596
Jaffe, D. T., Hildebrand, R. H., Keene, J., & Whitcomb, S. E. 1983, ApJ, 273, L89
Kogut, A., Smoot, G. F., Bennett, C. L., & Petuchowski, S. J. 1989, ApJ, 346, 763
Lane, A. P., Haas, M. R., Hollenbach, D. J., & Erickson, E. F. 1990, ApJ, 361, 132
Leach, R. W., Clemens, D. P., Kane, B. D., & Barvainis, R. 1991, ApJ, 370, 257 (L91)
Martin, A. H. M. 1972, MNRAS, 157, 121
Mundt, R., Ray, T. P., Bührke, T., Raga, A. C., & Solf, J. 1990, A&A, 232, 37
Novak, G., Gonatas, D. P., Hildebrand, R. H., Platt, S. R., & Dragovan, M. 1989, ApJ, 345, 802 (N89)
Novak, G., Predmore, C. R., & Goldsmith, P. F. 1990, ApJ, 355, 166
Platt, S. R., Hildebrand, R. H., Pernic, R. J., Davidson, J. A., & Novak, G. 1991, PASP, 1193 (P91)
Pudritz, R. E., & Norman, C. A. 1986, ApJ, 301, 571
Raymond, E., & Eliasson, B. 1969, ApJ, 155, 817
Schloerb, F. P., Snell, R. L., & Schwartz, P. R. 1987, ApJ, 319, 426 (SSS)
Scoville, N. Z., Sargent, A. I., Sanders, D. B., Claussen, M. J., Masson, C. R., Lo, K. Y., & Phillips, T. G. 1986, ApJ, 303, 416
Tamura, M., Hayashi, S. S., Yamashita, T., Duncan, W. D., & Hough, J. H. 1993, ApJ, 404, L21
Thronson, H. A. 1986, ApJ, 306, 160
Thronson, H. A., & Harper, D. A. 1979, ApJ, 230, 133
Thronson, H. A., Lada, C. J., & Hewagama, T. 1985, ApJ, 297, 662
Troland, T. H., Crutcher, R. M., & Kazès, I. 1986, ApJ, 304, L57
Turner, B. E., Balick, B., Cudaback, D. D., Heiles, C., & Boyle, R. J. 1974, ApJ, 194, 279
Uchida, Y., & Shibata, K. 1985, PASJ, 37, 515
Vogel, S. N., Genzel, R., & Palmer, P. 1987, ApJ, 316, 243 (VGP)
Welch, W. J., Dreher, J. W., Jackson, J. M., Tereby, S., & Vogel, S. N. 1987, Science, 238, 1550
Werner, M. W., et al. 1980, ApJ, 242, 601
Westbrook, W. E., Werner, M. W., Elias, J. H., Gezari, D. Y., Hauser, M. G., Lo, K. Y., & Neugebauer, G. 1976, ApJ, 209, 94
Wynn-Williams, C. G., Becklin, E. E., & Neugebauer, G. 1974, ApJ, 187, 473